A&A 606, A109 (2017)
DOI: 10.1051/0004-6361/201731405

Astronomy & Astrophysics

Detection of CH^+, SH^+, and their ^{13}C- and ^{34}S-isotopologues toward PKS 1830−211

S. Muller[1], H. S. P. Müller[2], J. H. Black[1], M. Gérin[3], F. Combes[4], S. Curran[5], E. Falgarone[3], M. Guélin[6,3], C. Henkel[7,8], S. Martín[9,10], K. M. Menten[7], E. Roueff[3], S. Aalto[1], A. Beelen[11], T. Wiklind[12], and M. A. Zwaan[13]

[1] Department of Space, Earth and Environment, Chalmers University of Technology, Onsala Space Observatory, 43992 Onsala, Sweden
e-mail: mullers@chalmers.se
[2] I. Physikalisches Institut, Universität zu Köln, Zülpicher Str. 77, 50937 Köln, Germany
[3] LERMA/LRA, École Normale Supérieure, Observatoire de Paris, CNRS UMR 8112, PSL Research University, Sorbonne Universités, UPMC Université Paris, 24 rue Lhomond, 75005 Paris, France
[4] Observatoire de Paris, LERMA, Collège de France, CNRS, PSL Univ., UPMC, Sorbonne Univ., 75014 Paris, France
[5] School of Chemical and Physical Sciences, Victoria University of Wellington, PO Box 600, 6140 Wellington, New Zealand
[6] Institut de Radioastronomie Millimétrique, 300 rue de la piscine, 38406 St Martin d'Hères, France
[7] Max-Planck-Institut für Radioastonomie, Auf dem Hügel 69, 53121 Bonn, Germany
[8] Astron. Dept., King Abdulaziz University, PO Box 80203, 21589 Jeddah, Saudi Arabia
[9] European Southern Observatory, Alonso de Córdova 3107, Vitacura, Casilla 19001, Santiago, Chile
[10] Joint ALMA Observatory, Alonso de Córdova 3107, Vitacura, 7630355 Santiago, Chile
[11] Institut d'Astrophysique Spatiale, Bât. 121, Université Paris-Sud, 91405 Orsay Cedex, France
[12] Department of Physics, Catholic University of America, 620 Michigan Ave NE, Washington DC 20064, USA
[13] European Southern Observatory, Karl-Schwarzschild-Str. 2, 85748 Garching b. München, Germany

Received 19 June 2017 / Accepted 21 July 2017

ABSTRACT

The $z = 0.89$ molecular absorber toward PKS 1830−211 provides us with the opportunity to probe the chemical and physical properties of the interstellar medium in the disk of a galaxy at a look-back time of half the present age of the Universe. Recent ALMA observations of hydrides have unveiled the multi-phase composition of this source's interstellar medium along two absorbing sightlines. Here, we report ALMA observations of CH^+ and SH^+, and of their ^{13}C- and ^{34}S-isotopologues, as potential tracers of energetic processes in the interstellar medium. CH^+ and $^{13}CH^+$ are detected toward both images of PKS 1830−211, CH^+ showing the deepest and broadest absorption among all species observed so far. The $[CH^+]/[^{13}CH^+]$ abundance ratio is ∼100 in the south-west line of sight. This value is larger than any previous $[^{12}CX]/[^{13}CX]$ ratios determined from other species toward this source and suggests either that the latter might be affected by fractionation or that CH^+ might be tracing a different gas component. Toward the north-east image, we find an even larger value of $[CH^+]/[^{13}CH^+]$, 146 ± 43, although with a large uncertainty. This sightline intercepts the absorber at a larger galactocentric radius than the southwestern one, where material might be less processed in stellar nucleosynthesis. In contrast to CH^+ and its ^{13}C isotopologue, SH^+ and $^{34}SH^+$ are only detected on the south-west sightline. These are the first detections of extragalactic SH^+ and interstellar $^{34}SH^+$. The spectroscopic parameters of SH^+ are reevaluated and improved rest frequencies of $^{34}SH^+$ are obtained. The $[CH^+]/[SH^+]$ column density ratios show a large difference between the two lines of sight: ∼25 and >600 toward the SW and NE image, respectively. We are not able to shed light on the formation process of CH^+ and SH^+ with these data, but the differences between the two sightlines toward PKS 1830−211 suggest that their absorptions arise from gas with a molecular fraction of $\gtrsim$10%, with SH^+ tracing significantly higher molecular fractions than CH^+.

Key words. quasars: absorption lines – quasars: individual: PKS 1830–211 – galaxies: ISM – galaxies: abundances – ISM: molecules – radio lines: galaxies

1. Introduction

Hydrides are formed by the first chemical reactions starting from atomic gas and are therefore at the root of interstellar chemistry. Due to the relative simplicity of their chemical network, they provide excellent diagnostics of the physico-chemical properties of the interstellar gas, especially of the low-density diffuse component (Gérin et al. 2016).

Methylidynium, CH^+, was one of the first interstellar molecules to be identified, in absorption in the optical spectrum toward bright stars (Douglas & Herzberg 1941). This discovery established a long-lasting problem for astrochemistry, the formation and survival of this reactive species in the interstellar medium (ISM). Its large observed abundances are at odds with predictions from steady-state quiescent gas-phase chemical models by several orders of magnitude. The formation path of the molecule, $C^+ + H_2 \rightarrow CH^+ + H$, has a high endothermicity of $\Delta E/k \sim 4300$ K, and mechanisms such as shocks (e.g., Elitzur & Watson 1980), dissipation of turbulence (e.g., Godard et al. 2009, 2014), intense FUV or X-ray radiation (e.g., Morris et al. 2016), or formation from vibrationally excited H_2 (e.g., Agúndez et al. 2010; Nagy et al. 2013; Faure et al. 2017) are advocated to overcome this problem.

The $J = 1$–0 transition of CH^+ (and its ^{13}C isotopologue), at 835 GHz (830 GHz, respectively), has been observed in absorption in Galactic sightlines toward massive

star-forming regions with the *Herschel* Space Observatory (Falgarone et al. 2010; Godard et al. 2012). In addition, optical absorption lines of CH^+ have been observed toward stars in the Magellanic Clouds (Welty et al. 2006) and even bright supernovae outside the Local Group (SN1986G in NGC 5128, D'Odorico et al. 1989; SN2006X in M 100, Cox & Patat 2008; SN2008fp in ESO 428−G14, Cox & Patat 2014; SN2014J in M 82, Ritchey et al. 2015), allowing us to probe extragalactic ISM lines of sight.

The sulfanylium ion SH^+ has an even higher endothermicity of $\Delta E/k \sim 9900$ K in its formation via the reaction of S^+ with ground-state H_2. SH^+ can also be formed by reactions of S^+ with vibrationally excited $H_2(v > 1)$ (Zanchet et al. 2013) and in X-ray dominated regions by reactions of S^{++} with H_2 (Abel et al. 2008). SH^+ was first detected in space in emission toward the massive star forming region W3 IRS5 (Benz et al. 2010) with the *Herschel* Space Observatory and in absorption toward the star-forming region complex Sgr B2 near the Galactic Center (Menten et al. 2011) with the Atacama Pathfinder EXperiment telescope (APEX). Unlike CH^+, it has never been detected in an extragalactic source before.

Because the formation of CH^+ and SH^+ have different endothermicity, their abundance ratio could reflect the physical properties of the region where these molecules form. Godard et al. (2012) did a comparative study of the CH^+ and SH^+ absorptions along multiple Galactic sightlines, and found that the CH^+/SH^+ column density ratios can vary by more than two orders of magnitude, from one to more than 100. They find, however, a relatively good correlation between $N(CH^+)/N(SH^+)$ and $N(CH^+)/N(H)$, except toward the Central Molecular Zone in the Milky Way. There, they argue that the stronger X-ray radiation field could trigger reactions of C^{++} and S^{++} ions with H_2 to enhance the abundances of CH^+ and SH^+.

Here, we report the detection of CH^+, SH^+, and their ^{13}C- and ^{34}S-isotopologues in the $z = 0.89$ absorber located in front of the quasar PKS 1830−211. The quasar, at $z = 2.5$ (Lidman et al. 1999), is gravitationally lensed by the foreground absorber, a nearly face-on spiral galaxy (Winn et al. 2002). The directions to the two bright and compact lensed images of the quasar (separated by 1″) form two independent lines of sight through the disk of the intervening galaxy, with absorption detected for many molecular species (e.g., Wiklind & Combes 1996; Muller et al. 2011, 2014a).

2. Observations

The observations were carried out with the Atacama Large Millimeter/submillimeter Array (ALMA) during its early cycles (1 and 2).

CH^+ tuning: the CH^+ and $^{13}CH^+$ $J = 1$–0 transitions, redshifted to ∼440 GHz in ALMA band 8, were observed simultaneously on 2015 May 20. The weather conditions were excellent, with a precipitable water vapor content of ∼0.3 mm. The total on-source time was approximately 17 min. The array was composed of 35 antennas, resulting in a synthesized beam of ∼0.3″, full-width at half maximum (FWHM). Hence, the two lensed images of PKS 1830−211 were well resolved. The correlator was configured with 1.875 GHz wide spectral windows and a spectral resolution of 1.1 MHz, corresponding to a velocity resolution, after Hanning smoothing, of ∼0.8 km s^{-1}.

SH^+ tuning: the SH^+ and $^{34}SH^+$ $N_J = 1_2$–0_1 transitions, redshifted to ∼280 GHz in ALMA band 7, were observed on 2014 May 5 (two executions) and July 18 (one execution). The $H_2^{18}O$ (1_{10}–1_{01}) line (rest frequency 547.676 GHz, redshifted to 290.4 GHz) was also observed with the same tuning. The weather conditions were good to moderate, with a precipitable water vapor content between 0.5–2.5 mm. The total on-source time comprised about one hour. In each execution, the array was composed of 30 antennas, resulting in a final synthesized beam smaller than 0.5″ *FWHM*. The correlator was also configured with 1.875 GHz wide spectral windows and a spectral resolution of 1.1 MHz, corresponding to a velocity resolution, after Hanning smoothing, of ∼1.2 km s^{-1}.

For both the CH^+ and the SH^+ tunings, the data calibration was done within the CASA[1] package, following a standard procedure. The bandpass response of the antennas was calibrated from observations of the bright quasar J 1924−292. The gain solutions were self-calibrated on the continuum of PKS 1830−211. The final spectra were extracted toward both lensed images of PKS 1830−211 using the CASA-python task UVMULTIFIT (Martí-Vidal et al. 2014) and fitting a model of two point sources to the interferometric visibilities.

3. Laboratory spectroscopic data

The spectroscopic parameters for the CH^+ and SH^+ lines discussed in this paper are given in Table 1. The CH^+ and $^{13}CH^+$ rest frequencies were taken from the Cologne Database for Molecular Spectroscopy (CDMS)[2] (Müller et al. 2001, 2005), based on Müller (2010). Both $J = 1$–0 transition frequencies were determined by Amano (2010). The rest frequencies for the SH^+ $N_J = 1_2$–0_1 transitions were taken from laboratory measurements by Halfen & Ziurys (2015). The CDMS SH^+ entry is based on the present work as detailed in Appendix A.

In the Born-Oppenheimer approximation, the SH^+ spectroscopic data can be taken directly to derive rest frequencies of $^{34}SH^+$ (Brown et al. 1986), see also Müller et al. (2015b) for the determination of NO spectroscopic parameters from data of several isotopic variants and references therein for further examples. The resulting $^{34}SH^+$ $N = 1$–0 transition frequencies are given in Table 2. Deviations from the Born-Oppenheimer approximation are not known accurately but are small in the case of a substitution of ^{32}S by ^{34}S. Trial fits with plausible values suggest that the most important correction, the one to the rotational constant B, may shift all $N = 1$–0 transition frequencies by around 1 MHz, usually, but not always, to higher frequencies. The correction to the spin-spin coupling parameter λ may cause shifts of around one to a few megahertz also, but affects mostly the upper and lower frequency FS components in opposite directions, whereas the shift of the $J = 2$−1 line is much smaller, possibly several 100 kHz. Other corrections as well as uncertainties from the values and uncertainties of the higher spectroscopic parameters are most likely smaller, but may add up to several 100 kHz.

We have adopted the electric dipole moment $\mu_{CH^+} = 1.68$ Debye (Cheng et al. 2007) and note that a nearly identical value $\mu_{^{13}CH^+} = 1.7$ Debye was reported for the heavier isotopologue (Follmeg et al. 1987). For the sulfanylium ion we have adopted the same value $\mu_{SH^+} = 1.28$ Debye for both isotopologues (Senekowitsch et al. 1985; Cheng et al. 2007).

4. Results

In this section, we present the absorption spectra of CH^+, $^{13}CH^+$, SH^+, and $^{34}SH^+$, obtained with ALMA toward the two lensed

[1] http://casa.nrao.edu/
[2] http://www.astro.uni-koeln.de/cdms/

Table 1. Line parameters.

Line	Observation date	Rest freq. (GHz)	Sky freq. (GHz)	E_{low} [a] (K)	S_{ul} [b]	α [c] (10^{12} cm^{-2} km^{-1} s)
SH^+ $N_J = 1_2$–0_1 $F = 1.5$–0.5	2014 May 05, Jul. 18	526.038793(50)	278.944	0.0	1.14	
$F = 2.5$–1.5	–	526.048023(50)	278.949	0.0	2.06	30.1
$F = 1.5$–1.5	–	526.124951(50)	278.990	0.0	0.23	
$^{34}SH^+$ $N_J = 1_2$–0_1	–	See dedicated entries in Table 2				
CH^+ $J = 1$–0	2015 May 20	835.137504(20)	442.851	0.0	1.0	2.85
$^{13}CH^+$ $J = 1$–0	–	830.216096(22)	440.241	0.0	1.0	2.79

Notes. Frequencies and molecular data are taken from the Cologne Database for Molecular Spectroscopy (Müller et al. 2001), except for $^{32}SH^+$, for which they are taken from direct laboratory measurements by Halfen & Ziurys (2015). See also Sect. 3. The sky frequencies were calculated using $z = 0.88582$ (heliocentric frame). [(a)] E_{low} is the lower-level energy of the transition. [(b)] S_{ul} is the line strength. [(c)] The coefficient α was defined in Eq. (2) and calculated under the assumption that the rotational excitation is coupled with the cosmic microwave background temperature, 5.14 K at $z = 0.89$ (see, e.g., Muller et al. 2013, 2014a). In case of hyperfine structure (SH^+), the coefficient applies to the hyperfine-structure deconvolved line profile, normalized for an equivalent component with $S_{ul} = 1$.

Table 2. Quantum numbers, frequencies, Einstein A coefficients, upper g_u and lower g_l state degeneracies, and upper E_u and lower E_l state energies of the $N = 1$–0 ground state rotational transition of $^{34}SH^+$.

$N' - N''$	$J' - J''$	$F' - F''$	Frequency[a] (MHz)	A (10^{-4} s^{-1})	g_u	g_l	E_u (cm^{-1})	E_l (cm^{-1})
1–0	0–1	0.5–0.5	344 896.7	1.14	2	2	11.5074	0.0029
	0–1	0.5–1.5	344 982.8	2.28	2	4	11.5074	0.0000
	2–1	1.5–0.5	525 085.2	7.95	4	2	17.5178	0.0029
	2–1	2.5–1.5	525 094.4	9.54	6	4	17.5153	0.0000
	2–1	1.5–1.5	525 171.4	1.59	4	4	17.5178	0.0000
	1–1	1.5–0.5	682 382.5	2.88	4	2	22.7647	0.0029
	1–1	0.5–0.5	682 408.4	11.53	2	2	22.7655	0.0029
	1–1	1.5–1.5	682 468.6	14.42	4	4	22.7647	0.0000
	1–1	0.5–1.5	682 494.5	5.77	2	4	22.7655	0.0000

Notes. [(a)] Uncertainties of at least ~2 MHz mostly because of a breakdown of the Born-Oppenheimer approximation, see Sect. 3.

images of PKS 1830−211. The spectra were first normalized to the continuum level of each image and are described as:

$$I_{abs}(v) = 1 - f_c \times \left[1 - \exp\left\{-\sum_i \tau_i(v)\right\}\right], \quad (1)$$

where f_c is the continuum source covering factor (i.e., the fraction of the continuum emission actually covered by the absorbing clouds) which can vary for different species, and $\tau_i(v)$, the optical depths of different velocity components, which we assume to have Gaussian profiles. In view of the following sections and Figs. 1–5, this choice of Gaussian profiles is a good approximation.

The size of the continuum emission at submillimeter wavelengths is as yet unknown, but Very Long Baseline Interferometry (VLBI) measurements at 7 mm indicate a size of ~0.2 mas for the southwest image, scaling linearly with λ (Jin et al. 2003). Projected in the plane of the absorber, the apparent sizes of the submm continuum images are thus ~0.1 pc in diameter. Since ALMA cannot spatially resolve this scale, the degeneracy between f_c and optical depth can only be broken for a heavily saturated line (as for CH^+), or possibly if spectrally resolved multiple fine and/or hyperfine components of different strengths allow us to constrain their opacity. In the absence of such constraints, we assumed $f_c = 1$ to derive apparent optical depths, and thus obtain lower limits to the column densities. From previous ALMA observations, Muller et al. (2014a) observed f_c(SW) between 91–95%, with a trend of increasing f_c with increasing frequency (i.e., when the size of the continuum emission becomes smaller). However, chemical segregation and time variations of the continuum morphology complicate the picture. The covering factor is unknown for the NE image, the OH^+ absorption observed by Muller et al. (2016) implying f_c(NE) > 50% in June 2015.

Next, we derived column densities by assuming that the excitation of CH^+ and SH^+ is strongly coupled to the cosmic microwave background (CMB, $T_{CMB} = 5.14$ K at $z = 0.89$, Muller et al. 2013) and that other contributions to the excitation are small. Although rotationally inelastic collisions with H, H_2, and e^- might need to be considered, reactive collisions of CH^+ with the same collision partners are even faster, so that the formation and destruction processes must be considered in proper analysis of the excitation (cf. Godard & Cernicharo 2013). Departures from the CMB can also be caused by radiative excitation in the local background radiation of the absorbing galaxy itself. We have no information about the local visible, infrared, and submm-wave continuum inside the absorbing galaxy. A local continuum comparable to that of the average background in the Milky Way would dominate the excess excitation of CH^+ in competition with collisions at the densities and temperatures of a Galactic diffuse molecular cloud. Even so, the excitation temperature in CH^+ $J = 1$–0 might be raised to ~6 K, which would still have a negligible effect on the following analysis.

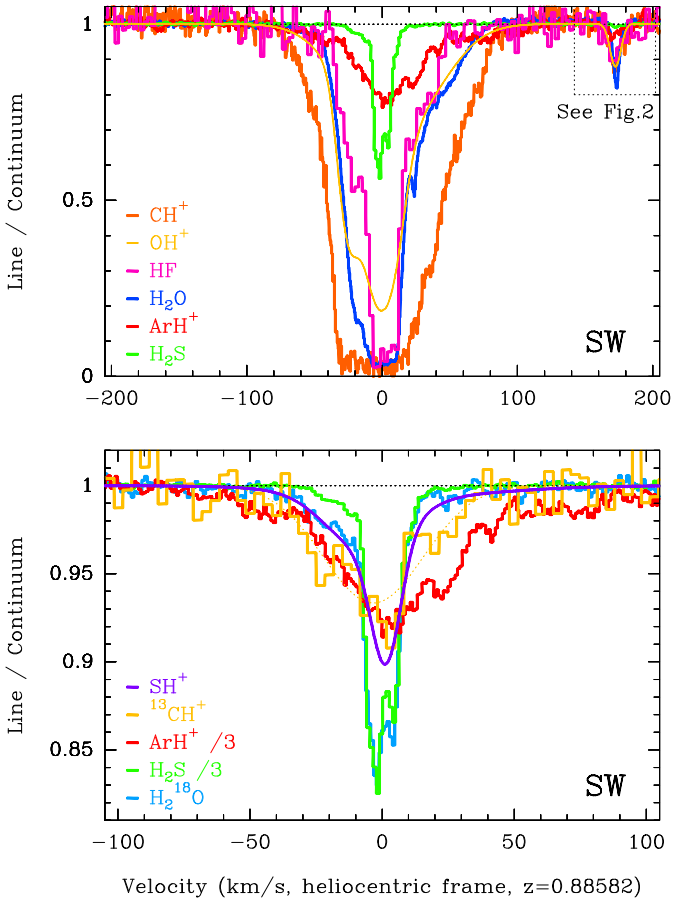

Fig. 1. Absorption spectra toward the southwest image of PKS 1830−211: *top*: of the CH^+ J = 1–0, OH^+ N = 1–0 (deconvolved from its hyperfine structure and shown for its strongest hyperfine component), HF J = 1–0, ortho-H_2O 1_{10}–1_{01}, ArH^+ J = 1–0, and para-H_2S 1_{11}–0_{00} lines; *bottom*: of the $^{13}CH^+$ J = 1–0, SH^+ N_J = 1_2–0_1 (deconvolved from its hyperfine structure and shown for its strongest hyperfine component), ArH^+ J = 1–0 (opacity scaled down by a factor of three), para-H_2S 1_{11}–0_{00} (opacity scaled down by a factor of three), and ortho-$H_2^{18}O$ 1_{10}–1_{01} lines. All spectra are normalized to the continuum level and are referenced to the heliocentric frame taking z = 0.88582.

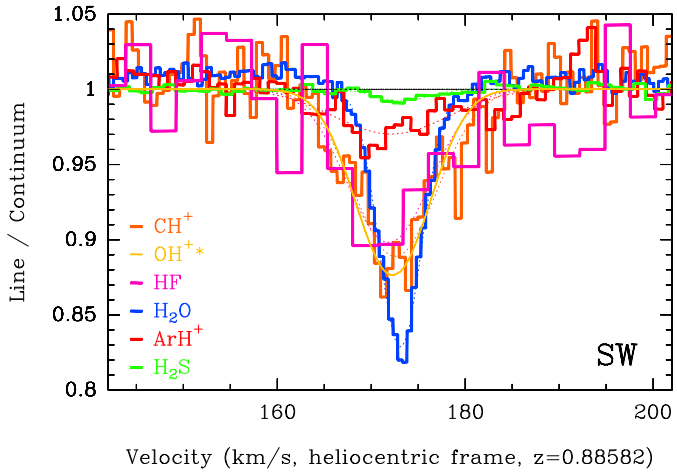

Fig. 2. Same as Fig. 1, upper panel, zoomed on the v = +170 km s^{-1} velocity component toward the southwest image. The dotted curves show the best fits with one Gaussian component.

Local excitation effects are unlikely to be any larger in SH^+ under diffuse-cloud conditions. Accordingly, we calculate the column densities as:

$$N_{\rm col} = \alpha_{ij} \times \int \tau_{ij} {\rm d}v, \quad (2)$$

where the α_{ij} coefficients (Table 1) are calculated for a given transition i–j for $T_{\rm rot}$ = 5.14 K (see e.g., Muller et al. 2014a).

4.1. PKS 1830−211 south-west line of sight

4.1.1. CH^+ and $^{13}CH^+$

Toward the SW image, the CH^+ spectrum shows deep and broad absorption (Fig. 1), the broadest of all molecular species observed so far at millimeter wavelengths toward this source (e.g., Muller et al. 2014a). The full width at zero power exceeds 160 km s^{-1}. The line appears flat-bottomed over a velocity range of ∼50 km s^{-1} (i.e., between −30 km s^{-1} and +20 km s^{-1}), although the absorption does not exactly reach the zero level, but implies a continuum source covering factor, f_c ∼ 97%. The covering factor is slightly higher than for saturated species observed before (Muller et al. 2014a). Most likely, this is due to the smaller continuum size at higher frequencies and/or to the intrinsic larger filling factor of CH^+, although we cannot exclude time variations (Muller & Guélin 2008).

The heavy saturation prevents us to derive directly the peak opacity of CH^+, its total column density, and chemical correlation with other species near v = 0 km s^{-1} velocities. By cutting the optical depths at a threshold of τ = 3, we estimate a lower limit of 6.4×10^{14} cm^{-2}. The weak v = +170 km s^{-1} component (Muller et al. 2011, 2014a) is also detected in CH^+, as shown in Fig. 2, with an apparent peak opacity of ∼0.1 and a *FWHM* ∼ 10 km s^{-1}, leading to a column density ∼4×10^{12} cm^{-2}.

The absorption from $^{13}CH^+$ is detected in the same tuning as CH^+ and barely reaches a depth of 10% of the continuum level near v = 0 km s^{-1}. The hyperfine splitting of the $^{13}CH^+$ J = 1−0 line is smaller than 2 MHz (rest frame), that is, spread over a velocity interval ∼0.7 km s^{-1}. This is much smaller than the FWHM of the line, and is thus neglected here. The total column density is about 9×10^{12} cm^{-2}.

We further discuss the CH^+ absorption in comparison with other species and the $[CH^+]/[^{13}CH^+]$ ratio in Sect. 5.

4.1.2. SH^+ and $^{34}SH^+$

The SH^+ absorption is detected near v = 0 km s^{-1} with an optical depth ∼0.15. The identification of SH^+ is corroborated by the presence of $^{34}SH^+$ at the expected frequency (see below and Sect. 3). Spectra for both isotopologues, converted into opacity scale, are shown in Fig. 3. The absorption profile of SH^+, deconvolved from its hyperfine structure and in velocity scale, is shown in Fig. 1. This profile was obtained by the fit of Gaussian velocity components convolved with the hyperfine structure. Only three Gaussian components are required to fit the profile, leaving residuals at the level of the noise, see Fig. 3. In particular, two Gaussian components are necessary to reproduce the large and asymmetric blue and red wings.

The companion absorption from $^{34}SH^+$ can also be included in the same fit. As an exercise to compare with spectroscopic calculations (see Sect. 3), we assume for $^{34}SH^+$ the same hyperfine structure as for SH^+ (i.e., same splitting and relative line intensities) but shifted in frequency by a constant value δ, and the same intrinsic velocity profile. We find δ = 952.5 ± 1.9 MHz,

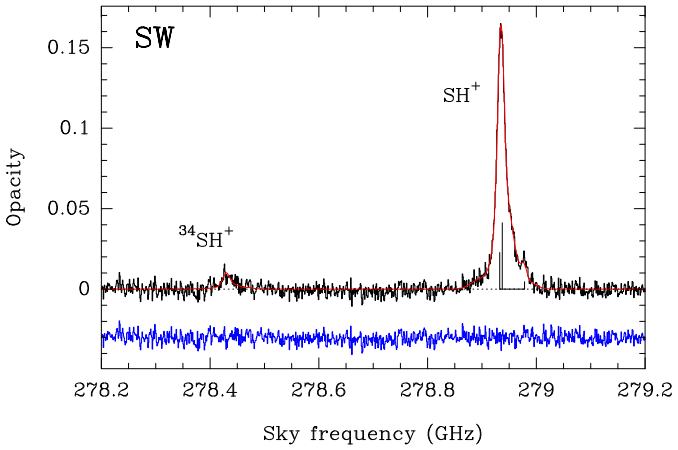

Fig. 3. Opacity spectra of the SH^+ and $^{34}SH^+$ lines toward the SW image of PKS 1830−211, shown with their best fit model (three Gaussian components convolved with the hyperfine structure, in red) and the fit residuals (in blue, offset by −0.03). The hyperfine structure is indicated for SH^+. We assumed the same hyperfine structure, shifted in frequency by a constant value for $^{34}SH^+$ (see Sect. 4.1.2).

consistent with but not providing more accurate values than the frequencies listed in Table 2. In this fit, we also find a ratio $SH^+/^{34}SH^+$ of 16.2 ± 1.3, slightly higher than the $^{32}S/^{34}S$ ratios obtained previously from CS ($10.4^{+0.8}_{-0.7}$) and H_2S (10.6 ± 0.9) isotopologues by Muller et al. (2006), but significantly smaller than the solar system value of 22 (Lodders 2003).

4.2. PKS 1830−211 north-east line of sight

4.2.1. CH^+ and $^{13}CH^+$

The CH^+ NE absorption profile consists of a series of individual velocity components, with widths as small as a few km s^{-1}, spanning the large continuous interval between −300 km s^{-1} and −100 km s^{-1} (Fig. 4). A fit of 12 Gaussian velocity components reproduces well the overall line opacity profile (see Fig. 5 and the list of velocity components in Table 3). The absorption reaches a depth of about 80% of the continuum level at $v \sim -156$ km s^{-1}, implying that the source covering factor f_c is >80% for this peak absorption. Without stronger constraints, we have assumed $f_c = 1$ toward this image. The total CH^+ column density is about 1.9×10^{14} cm^{-2}.

The $^{13}CH^+$ absorption is weakly detected. It is the first such detection for a ^{13}C isotopologue toward the NE image of PKS 1830−211. It reaches a depth of ∼1% of the continuum level. A simultaneous fit of the CH^+ and $^{13}CH^+$ spectra (with the same 12-Gaussian velocity components profile obtained above) yields a $[CH^+]/[^{13}CH^+]$ ratio of 146 ± 43. The total $^{13}CH^+$ column density is about 1.3×10^{12} cm^{-2} along the NE line of sight.

4.2.2. SH^+

Despite a sensitivity better than 0.2% of the continuum level, SH^+ is not detected toward the NE image. We have estimated an upper limit of the SH^+ integrated opacity as $3\sigma\sqrt{\delta V \times FWHM} = 0.036$ km s^{-1}, where we take the $FWHM = 42$ km s^{-1} determined from the fit of the CH^+ absorption with only one Gaussian velocity component, and where σ is the standard deviation of the spectrum and δV the velocity resolution. This corresponds to an upper limit of 3.2×10^{11} cm^{-2} for the column density. The abundance ratio between the SW and NE lines of sight, provided

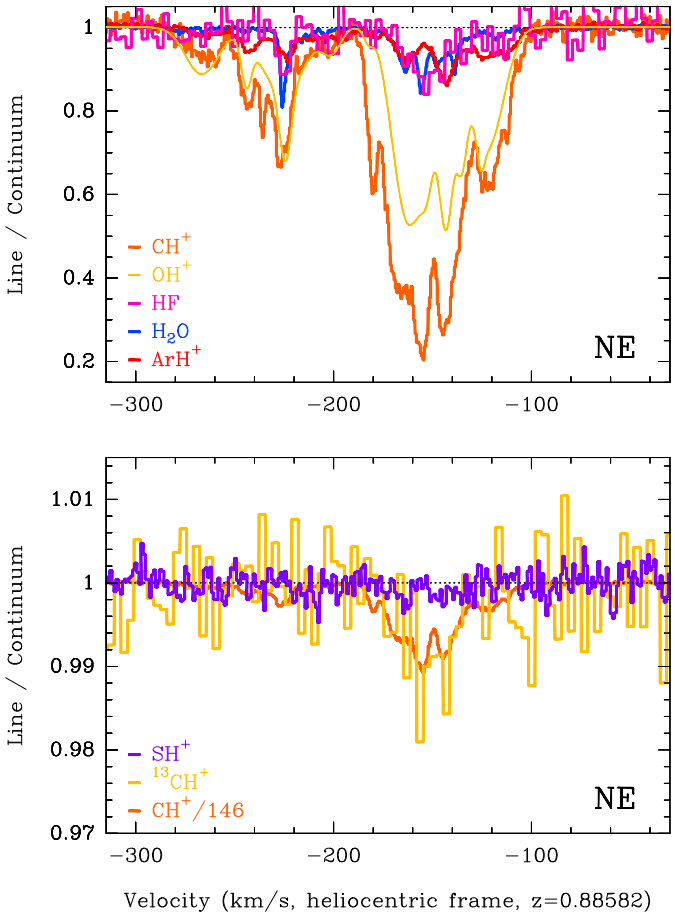

Fig. 4. Absorption spectra toward the northeast image of PKS 1830−211: *top*: of the CH^+ $J = 1$–0, OH^+ $N = 1$–0 (deconvolved from its hyperfine structure and shown for its strongest hyperfine component), HF $J = 1$–0, ortho-H_2O 1_{10}–1_{01}, and ArH^+ $J = 1$–0 lines; *bottom*: of the $^{13}CH^+$ $J = 1$–0, SH^+ $N_J = 1_2$–0_1 (deconvolved from its hyperfine structure and shown for its strongest hyperfine component), and CH^+ $J = 1$–0 (opacity scaled down by a factor of 146). All spectra are normalized to the continuum level and are referenced to the heliocentric frame taking $z = 0.88582$. The $^{13}CH^+$ spectrum was smoothed to 3.3 km s^{-1} for better signal-to-noise ratio (S/N) in individual channels.

excitation conditions are comparable, is then larger than 120, which is much higher than for other hydrides like ArH^+, OH^+, H_2O^+, H_2Cl^+, and CH^+ (see Table 4 and Sect. 5.2).

5. Discussion

5.1. Comparison with other species

5.1.1. Time variations

As previously shown (e.g., Muller & Guélin 2008; Schulz et al. 2015), we have to account for the effect of time variations for the comparison of spectra taken at different epochs toward PKS 1830−211, with an observed timescale of the order of one month to several years. The lensing geometry of the system is such that morphological changes in the background quasar, for example due to the emission of new plasmons in the (possibly helical) jet (Garrett et al. 1997; Jin et al. 2003; Nair et al. 2005), can cause a slightly varying illumination of clouds in the absorber and thereby changes in the absorption line profiles toward both lensed images.

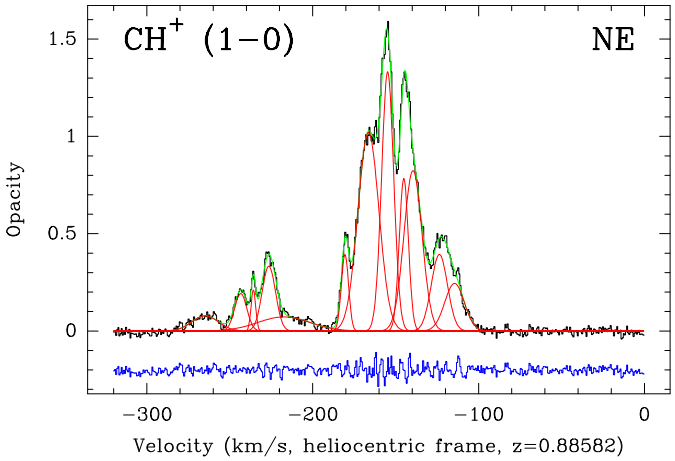

Fig. 5. Fit of the CH^+ J = 1–0 line opacity profile toward the NE image of PKS 1830−211. The individual Gaussian components (listed in Table 3) are marked in red and the global resulting profile is shown in green. The fit residuals are shown in blue, offset by −0.2 in opacity.

Table 3. Gaussian velocity components used to fit the CH^+ opacity profile toward the NE image of PKS 1830−211, as shown in Fig. 5.

v_0 (km s^{-1})	$FWHM$ (km s^{-1})	$\int \tau dv$ (km s^{-1})
−264.9 ± 1.3	18.6 ± 2.6	1.6 ± 0.3
−243.4 ± 0.3	8.6 ± 1.2	1.8 ± 0.6
−235.8 ± 0.1	3.3 ± 0.4	0.7 ± 0.1
−226.5 ± 0.2	9.5 ± 0.9	3.4 ± 0.7
−217.4 ± 9.6	40.0 ± 13.3	2.9 ± 1.6
−180.6 ± 0.1	5.1 ± 0.2	2.1 ± 0.1
−166.4 ± 0.2	14.9 ± 0.5	16.2 ± 0.6
−154.8 ± 0.2	8.5 ± 0.4	12.1 ± 1.1
−145.1 ± 0.1	6.5 ± 0.9	5.4 ± 3.1
−139.6 ± 1.8	12.8 ± 3.4	11.2 ± 4.4
−123.6 ± 1.4	11.5 ± 2.9	4.8 ± 3.3
−114.5 ± 4.3	13.8 ± 3.9	3.6 ± 2.8

We do not expect micro-lensing, for example, by a stellar-mass object in the lens plane, to cause effective variability, because the continuum emitting size of the quasar at mm wavelengths is still several orders of magnitude larger than the corresponding Einstein radius, $\theta_{\rm E,micro} \sim 2$ μas. A transverse velocity ∼1000 km s^{-1} in the lens plane would convert into an apparent drift of ∼0.5 mpc within one year. The timescale associated with milli-lensing by an object of $\gg 1$ $M_\odot$ would thus be of the order of weeks or longer.

ArH^+ (Müller et al. 2015a) and HF (Kawaguchi et al. 2016) were observed by ALMA the day before CH^+ in May 2015, while OH^+ was observed about two weeks later (Muller et al. 2016). In May and July 2014, the ground-state transitions of ortho-$H_2^{18}O$ were observed in the same tuning as SH^+, and another sulfur-bearing molecule, para-H_2S, was observed within one month. Within such short time intervals, we do not expect significant variations of the absorption profiles.

Muller et al. (2016) discuss the temporal variations of H_2O, CH, and H_2O^+ profiles between the different ALMA observing sessions in 2014, 2015, and 2016. The major changes occur in the blue and red wings of the saturated line of H_2O toward the SW image, with an increase of ∼50% of the integrated opacities in the velocity ranges −60 to −20 km s^{-1} and +20 to +80 km s^{-1} between 2014 and 2016. For CH, the total integrated opacity varies by less than 6%. Toward the NE image, the total integrated opacity of the water line varies by less than 15% in this period. Different fine structure transitions of H_2O^+, observed between 2014 and 2015, do not show significant differences. These checks have allowed us to link the profiles of the different species observed with ALMA between 2014 and 2015, and suggest little evolution of the absorption line profiles toward the two images of PKS 1830−211 during this period.

Allison et al. (2017) recently published a study of the long-term variability of the 21 cm H I line toward PKS 1830−211. They compare the H I profiles observed in 1996 by Chengalur et al. (1999) and 1999 by Koopmans & de Bruyn (2005) with new data obtained in 2014–2015. In stark contrast with the molecular variability at millimeter wavelengths, they find only marginal variations of at most few percent within this long time span. This is consistent with the fact that the continuum at cm wavelengths is much more extended, smoothing away all variations. In the absence of better estimates of H I column densities, we used those derived from the source kinematical model by Koopmans & de Bruyn (2005) and given in Table 4 (see also Muller et al. 2016).

5.1.2. Column density ratios

Among the species used for comparison in this paper, only OH^+, and ArH^+ have wings sufficiently broad toward the SW image to avoid the saturated region in the CH^+ spectrum and are strong enough toward the NE image, for determining column density ratios with CH^+. These ratios are shown in Fig. 6 for both lines of sight. The $[OH^+]/[CH^+]$ ratio is rather constant, $=1.8 \pm 0.2$, in the wings of the SW absorption (v = −60 to −40 km s^{-1} and +20 to +80 km s^{-1}), but varies significantly between ∼1 and 18 for all other velocities of the NE absorption (v = −300 to −100 km s^{-1}). It is ∼9 for the v = +170 km s^{-1} component toward the SW image. On the other hand, the $[CH^+]/[ArH^+]$ ratio is varying abruptly between ∼2 and 60, and never stabilizes to a constant value. We note a clear trend that when $[OH^+]/[CH^+]$ is low, $[CH^+]/[ArH^+]$ is high, and vice versa, one possible explanation being that CH^+ traces gas with higher f_{H2} than ArH^+ and OH^+.

Assuming that the $[OH^+]/[CH^+]$ ratio is constant over the SW absorption, that is, also in the saturated region of the CH^+ absorption, we can perform a simultaneous fit of the CH^+, $^{13}CH^+$, and OH^+ spectra, using Eq. (1) with a single intrinsic velocity profile for all species. The free parameters of the fit are thus the centroid velocity, FWHM, and integrated opacity for each Gaussian velocity component, the source covering factor, f_c (we assumed the same for each species), and the scaling factors between species. The best fit with three Gaussian components yields f_c = 97.8 ± 0.3%, $[CH^+]/[^{13}CH^+]$ = 97 ± 6, and $[OH^+]/[CH^+]$ = 1.7 ± 0.1. It reproduces the spectra well and leaves residuals close to the noise level. For simplicity, we assumed Gaussian statistics on the errors in the fit. From this, we derive a new "saturation-corrected" total column density for CH^+ of 9.7×10^{14} cm^{-2}. Using the H I and H_2 column densities from Table 4, we finally obtained the CH^+ abundance relative to total hydrogen: $N(CH^+)/N(H)$ = $N(CH^+)/(N(H\,I) + 2 \times N(H_2))$ = 2×10^{-8} and 4×10^{-8} along the SW and NE lines of sight, respectively, comparable to typical values found in the Milky Way (e.g., Falgarone et al. 2010; Menten et al. 2011; Godard et al. 2012).

In Fig. 7, we show the column density ratios of SH^+ relative to other species discussed in this work, for the SW line of sight. These ratios show a clear pattern with different species and

Table 4. Total column densities of various species along the SW and NE lines of sight toward PKS 1830−211.

Species	Observation year	Column densities (cm^{-2}) SW	NE	$\gamma_{SW/NE}$	f_{H2}
H I	1996–2015[a]	1.3×10^{21}	2.5×10^{21}	0.5	~1–>50%
ArH^+	2015[b]	2.7×10^{13}	1.3×10^{13}	2.1	10^{-5}–10^{-2}[j]
OH^+	2015[c]	1.6×10^{15}	7.6×10^{14}	2.2	a few %
H_2Cl^+	2012[d]	1.4×10^{13}	3.7×10^{12}	3.8	
H_2O^+	2014[c]	2.7×10^{14}	7.0×10^{13}	3.9	a few %
CH^+	2015[e]	9.7×10^{14}	1.9×10^{14}	5.1	
$^{13}CH^+$	2015[e]	9.8×10^{12}	1.3×10^{12}	7.5	
HF	2015[f]	$>3.4 \times 10^{14}$	1.8×10^{13}	>19	
CH	2012[g]	7.7×10^{14}	3.5×10^{13}	22.	~10–100%
HCO^+	2009[h]	1.8×10^{14}	7.5×10^{12}	23.	
HCN	2009[h]	3.0×10^{14}	7.3×10^{12}	42.	
C_2H	2009[h]	1.2×10^{15}	2.9×10^{13}	43.	
c-C_3H_2	2009[h]	5.3×10^{13}	1.2×10^{12}	44.	
N_2H^+	2009[h]	2.3×10^{13}	$<0.3 \times 10^{12}$	>70	
o-$H_2^{18}O$	2014[e]	1.5×10^{13}	$<1.8 \times 10^{11}$	>82	
HNC	2009[h]	1.0×10^{14}	1.2×10^{12}	87	
SH^+	2014[e]	3.9×10^{13}	$<3.2 \times 10^{11}$	>120	
p-H_2S	2014[e]	6.6×10^{13}	$<4.8 \times 10^{11}$	>140	
H_2	2012[g,i]	$\sim 2 \times 10^{22}$	$\sim 1 \times 10^{21}$	~20	

Notes. Species are ordered with increasing SW/NE column density ratios, $\gamma_{SW/NE}$. We note that time variations might affect the comparison of data observed far apart in time.

References. [(a)] Chengalur et al. (1999), Koopmans & de Bruyn (2005), Allison et al. (2017); [(b)] Müller et al. (2015a); [(c)] Muller et al. (2016); [(d)] Muller et al. (2014b); [(e)] this work; [(f)] Kawaguchi et al. (2016); [(g)] Muller et al. (2014a); [(h)] Muller et al. (2011); [(i)] the column densities of H_2 were derived using CH and H_2O as proxies (Muller et al. 2014a); [(j)] Schilke et al. (2014), Neufeld & Wolfire (2016).

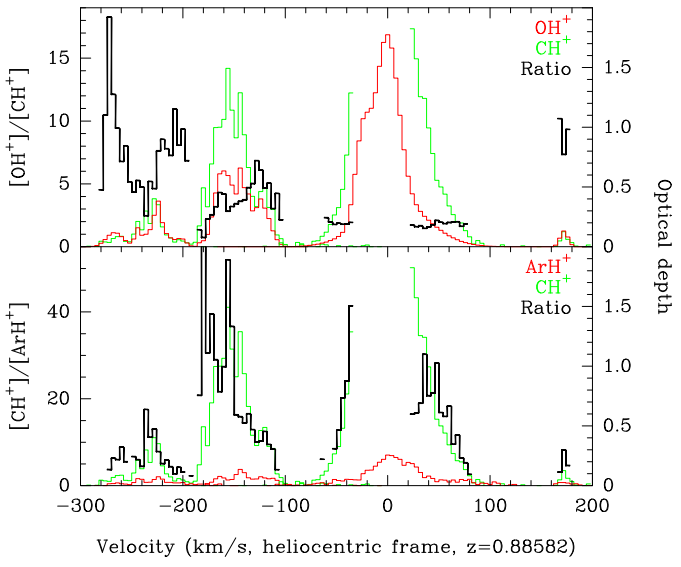

Fig. 6. Column density ratios of $[OH^+]/[CH^+]$ (*top*) and $[CH^+]/[ArH^+]$ (*bottom*) toward the NE ($v < -100$ km s^{-1}) and SW ($v > -100$ km s^{-1}) lines of sight. The ratios are shown in black curves. The green and red curves are optical depths and translate into column densities with factors 2.85×10^{12}, 20.0×10^{12}, and 1.70×10^{12} cm^{-2} km^{-1} s for CH^+, OH^+, and ArH^+, respectively. Channels with S/N < 3 or opacity larger than 2 were flagged prior to calculate the ratios.

velocity ranges. At $|v| < 10$ km s^{-1}, the ratios $[X]/[SH^+]$ go to a minimum for $X = OH^+$, H_2O^+, $^{13}CH^+$, and ArH^+, all hydrides preferentially tracing gas with low molecular fraction. The ratios increase by a factor two or more in the wings, for $|v| > 10$ km s^{-1}. For X = ortho-$H_2^{18}O$ and para-H_2S, the ratios show a reverse trend in the velocity interval $|v| < 10$ km s^{-1}, increasing toward the line center and dropping by a factor two or more in the wings. The $|v| < 10$ km s^{-1} velocity interval is dominated by translucent gas with a relatively high density of a few 10^3 cm^{-3}, as determined from the excitation of NH_3 (Henkel et al. 2008) and several other species (Henkel et al. 2009; Muller et al. 2013). In the line wings, where the low-f_{H2} tracers show enhanced absorption, the density is likely lower and the gas more diffuse. Hence, we can conclude that SH^+ behaves intermediate between tracers of low- and high-molecular fraction, in agreement with the analysis by Neufeld et al. (2015) along Galactic sightlines.

Taking the total column densities, we find a large difference in the $[CH^+]/[SH^+]$ ratios between the two lines of sight toward PKS 1830−211: ~25 toward the SW image and >600 toward the NE. This agrees with the correlation derived by Godard et al. (2012) in the Milky Way, that shows a higher $N(CH^+)/N(SH^+)$ ratio in regions with high $N(CH^+)/N(H)$. However, the difference of $N(CH^+)/N(H)$ between the two PKS 1830−211 sightlines is only a factor of two, when the $[CH^+]/[SH^+]$ varies by a factor >24. The $[CH^+]/[SH^+]$ ratios collected by Godard et al. (2012) show a large scatter of more than two orders of magnitude. They interpret these wild variations as linked to the ion-drift velocity in the turbulent dissipation regions model, therefore the amount of suprathermal energy injected in the system, and to the difference in formation endothermicities between the two species.

5.2. Comparison of the two lines of sight toward PKS 1830−211

CH^+, SH^+, and their ^{13}C- and ^{34}S-isotopologues are detected toward the SW image of PKS 1830−211. This line of sight is known to contain nearly 50 molecular species, not counting

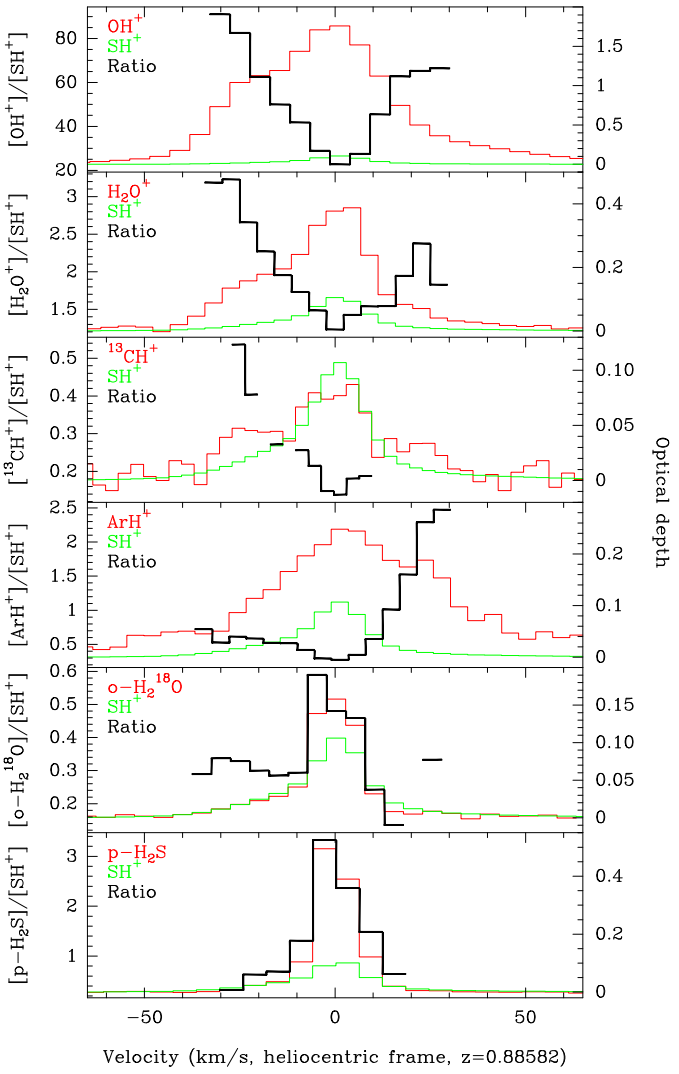

Fig. 7. Column density ratios (in black) of several species (in red) relative to SH^+ (in green) toward the SW image of PKS 1830−211. Opacity spectra were smoothed by five channels to improve the S/N in individual channels. The column density ratios are calculated only where both species have opacity S/N larger than five.

isotopologues, with an H_2 column density of about 2×10^{22} cm^{-2} (see, e.g., Muller et al. 2011, 2014a). At $v \sim 0$ km s^{-1}, it mostly consists of translucent clouds at moderate density of the order of 10^3 cm^{-3} and with a kinetic temperature of ~80 K (Henkel et al. 2009; Muller et al. 2013). In contrast, the NE line of sight consists of more diffuse gas (see e.g., Muller & Guélin 2008; Muller et al. 2014b, 2016), although the physical conditions are not as well constrained as toward the SW image.

Previously, four species have been found to have enhanced abundances in the NE line of sight, with respect to the SW line of sight: H_2Cl^+ (Muller et al. 2014b), ArH^+ (Müller et al. 2015a), and OH^+ and H_2O^+ (Muller et al. 2016). These species are also known to trace gas with low molecular fraction (Gérin et al. 2016). Muller et al. (2016) noticed that the total column density ratio between the SW and NE images (hereafter $\gamma_{SW/NE}$) for a given species is a good indicator of what kind of gas it preferentially traces. We list in Table 4 the column densities of several species observed toward both lines of sight, as well as their $\gamma_{SW/NE}$ ratios. When ordered with increasing value of $\gamma_{SW/NE}$, there is a clear trend with tracers of increasing f_{H2}.

In this picture, CH^+, with a $\gamma_{SW/NE} = 5$, is intermediate between the low f_{H2} tracers, for example OH^+ and H_2O^+ (tracing f_{H2} of a few percent) and high f_{H2} tracers, such as CH and HF, for which $\gamma_{SW/NE} \gtrsim 20$. On the other hand, SH^+, with its non detection in the NE line of sight, yields a lower limit $\gamma_{SW/NE} > 120$, a rather extreme ratio among the species listed, either suggesting that SH^+ is found in gas with relatively high-f_{H2} or that the physical conditions in the NE line of sight are not favorable to the formation of SH^+. By comparison, Godard et al. (2012) find molecular fractions with a large scatter $0.04 < f_{H2} < 1$ for the diffuse gas seen in CH^+ and SH^+ absorption along Galactic sightlines, with an average value of 10%.

In their recent chemical predictions, Neufeld & Wolfire (2016) find a sequence ArH^+–HCl^+–H_2Cl^+–OH^+–H_2O^+ where the five ions reach their peak abundance at increasing molecular fraction (or visual extinction). ArH^+ is confirmed to be a unique tracer of almost purely atomic gas (i.e., even better than H I), peaking at molecular fraction 10^{-5}–10^{-2} (see also Schilke et al. 2014). OH^+ and H_2O^+ are found to reside primarily in gas with $f_{H2} \sim 0.01$–0.1, with the chlorine-bearing ions tracing intermediate $f_{H2} \lesssim 0.1$. Although not perfect, the agreement between the $\gamma_{SW/NE}$-classification from the two PKS 1830−211 sightlines and the chemical predictions is remarkable.

Finally, we note that the $[CH^+]/[CH]$ ratio in the NE line of sight is higher (~5) than in the SW (~1). In the Milky Way, an elevated $[CH^+]/[CH]$ ratio suggests a larger contribution of the CH^+ chemistry to the formation of CH, in contrast to regions where relatively more CH arises from quiescent chemistry, as discussed by Federman et al. (1997) and Porras et al. (2014).

5.3. $^{12}C/^{13}C$ ratio

Because of its relatively large value (~60 in the local ISM, Lucas & Liszt 1998), the interstellar $^{12}C/^{13}C$ ratio can be difficult to measure, either due to saturation of the main ^{12}C-species or sensitivity issues with the detection of the ^{13}C-isotopologues. In addition, the interpretation of the $[^{12}CX]/[^{13}CX]$ abundance ratio can be complicated by fractionation and/or selective photodissociation. From optical-line absorption studies in the Milky Way, Ritchey et al. (2011) find that the $[^{12}CH^+]/[^{13}CH^+]$ ratio does not deviate from the $^{12}C/^{13}C$ isotopic ratio, as expected if the molecule forms via energetic processes.

Our measurement of $[^{12}CH^+]/[^{13}CH^+]$ toward the SW image is indirect, using the $[OH^+]/[CH^+]$ ratio determined from the line wings to link CH^+ in the saturated velocity interval near $v = 0$ km s^{-1} to $^{13}CH^+$. We derive $[^{12}CH^+]/[^{13}CH^+] = 97 \pm 6$ in a combined fit, which would imply a large optical depth of between approximately five and ten for the peak of the CH^+ absorption. This $[^{12}CX]/[^{13}CX]$ ratio is much higher than the previous measurements ~30–40 using HCO^+, HCN, and HNC (Muller et al. 2006, 2011). Non detection of the ^{13}C-variants for H_2CO and C_2H sets limits to the ratio significantly higher than 40 (Muller et al. 2011), and may suggest fractionation issues (see e.g., Roueff et al. 2015). Alternatively, it could be possible that the isotopic ratio is different due to incomplete mixing between different gas components: low- vs. high-f_{H2} gas or molecular gas that has been more enriched by recent stellar formation vs. a more highly disturbed component of the ISM.

For the first time toward the NE image, we are able to measure a $[^{12}CX]/[^{13}CX]$ ratio. From a combined fit of the CH^+ and $^{13}CH^+$ spectra, we obtain $[^{12}CH^+]/[^{13}CH^+] = 146 \pm 43$. In this fit, we set the ratio as a free parameter and assume Gaussian statistics on the uncertainties. As for the $^{36}Ar/^{38}Ar$ ratio (Müller et al. 2015a), we find a slight difference between the two

lines of sight, suggesting that the NE lines of sight, intercepting the absorber at a galactocentric radius of ∼4 kpc compared to ∼2 kpc for the SW line of sight, might be composed of less processed material.

6. Summary and conclusions

We report ALMA observations of CH^+, SH^+, and their ^{13}C- and ^{34}S-isotopologues along two independent lines of sight, with different physico-chemical properties, across the $z = 0.89$ absorber toward PKS 1830−211. CH^+ shows deep absorption spanning a velocity range of ∼200 km s^{-1} along both sightlines, with $^{13}CH^+$ also detected, albeit weakly, along both. In contrast, SH^+ is only detected toward the SW line of sight, characterized by an higher average molecular fraction f_{H2}. We report the first interstellar detection of $^{34}SH^+$ in the same line of sight.

The $[CH^+]/[SH^+]$ column density ratios differ widely between the two sightlines, ∼25 in the SW, and >600 in the NE. This suggests, in agreement with previous observations, that SH^+ resides in gas with high f_{H2} ($\gtrsim$10%). Alternatively, the difference of column density ratios might be due to the difference of formation endothermicity between the two species, with physical conditions not as favorable to the formation of SH^+ in the NE line of sight.

We suggest that the total column density ratios between the two lines of sight for a given species is a good indicator of the molecular fraction where the species primarily resides. In this picture, CH^+ is placed in gas with $f_{H2} \gtrsim 10\%$, that is, with similar or possibly slightly higher f_{H2} than for OH^+ and H_2O^+. The CH^+ $J = 1$–0 line is the most heavily saturated line among all species previously observed in this source, and as such, appears as the best tracer of diffuse gas in terms of detectability, in particular at high redshift.

The detection of $^{13}CH^+$ allows us to estimate $[^{12}CH^+]/[^{13}CH^+] \sim 100$ and ∼150, toward the SW and NE sightlines, respectively. The SW value is larger than any previous $[^{12}CX]/[^{13}CX]$ ratios determined from HCO^+, HCN, and HNC. The even larger (although somewhat uncertain) value derived in the NE line of sight, intercepting the disk of the absorber at a larger galactocentric radius, suggests that the material might be less processed by stellar nucleosynthesis. This work shows that with the unprecedented sensitivity and frequency coverage of ALMA, we now have the opportunity to follow up the recent breakthroughs in our understandings of the physics and chemistry in the ISM of our Milky Way, with observations of hydrides in distant galaxies, and of the $z = 0.89$ absorber toward PKS 1830−211, in particular.

Acknowledgements. We thank the referee for useful comments and corrections. This paper makes use of the following ALMA data: ADS/JAO.ALMA#2012.1.00056.S and #2013.1.00020.S. ALMA is a partnership of ESO (representing its member states), NSF (USA) and NINS (Japan), together with NRC (Canada) and NSC and ASIAA (Taiwan) and KASI (Republic of Korea), in cooperation with the Republic of Chile. The Joint ALMA Observatory is operated by ESO, AUI/NRAO and NAOJ. This research has made use of NASA's Astrophysics Data System.

References

Abel, N. P., Federman, S. R., & Stancil, P. C. 2008, ApJ, 675, 81
Agúndez, M., Goicoechea, J. R., Cernicharo, J., Faure, A., & Roueff, E. 2010, ApJ, 713, 662
Allison, J. R., Moss, V. A., Macquart, J.-P., et al. 2017, MNRAS, 465, 4450
Amano, T. 2010, ApJ, 716, L1
Benz, A. O., Bruderer, S., van Dishoeck, E. F., et al. 2010, A&A, 521, L35
Brown, J. M., & Müller, H. S. P. 2009, J. Mol. Spectr., 255, 68
Brown, P. R., Davies, P. B., & Johnson, S. A. 1986, Chem. Phys. Lett., 132, 582
Cheng, M., Brown, J. M., Rosmus, P., et al. 2007, Phys. Rev. A, 75, 012502
Chengalur, J. N., de Bruyn, A. G., & Narasimha, D. 1999, A&A, 343, 79
Civiš, S., Blom, C. E., & Jensen, P. 1989, J. Mol. Spectr., 138, 69
Cox, N. L. J., & Patat, F. 2008, A&A, 485, 9
Cox, N. L. J., & Patat, F. 2014, A&A, 565, A61
D'Odorico, S., di Serego Alighieri, S., Pettini, M., et al. 1989, A&A, 215, 21
Douglas, A. E., & Herzberg, G. 1941, ApJ, 94, 381
Elitzur, M., & Watson, W. D. 1980, ApJ, 236, 172
Falgarone, E., Godard, B., Cernicharo, J., et al. 2010, A&A, 521, A15
Faure, A., Halvick, P., Stoecklin, T., et al. 2017, MNRAS, 469, 612
Federman, S. R., Welty, D. E., & Cardelli, J. A. 1997, ApJ, 481, 795
Follmeg, B., Rosmus, P., & Werner, H.-J. 1987, Chem. Phys. Lett., 136, 562
Garrett, M. A., Nair, S., Porcas, R. W., & Patnaik, A. R. 1997, Vist. Astron., 41, 281
Gérin, M., Neufeld, D., & Goicoechea, J. 2016, ARA&A, 54, 181
Godard, B., & Cernicharo, J. 2013, A&A, 550, A8
Godard, B., Falgarone, E., & Pineau Des Forêts, G. 2009, A&A, 495, 847
Godard, B., Falgarone, E., Gerin, M., et al. 2012, A&A, 540, A87
Godard, B., Falgarone, E., & Pineau Des Forêts, G. 2014, A&A, 570, A27
Halfen, D. T., & Ziurys, L. M. 2015, ApJ, 814, 119
Henkel, C., Braatz, J. A., Menten, K. M., & Ott, J. 2008, A&A, 485, 451
Henkel, C., Menten, K. M., Murphy, M. T., et al. 2009, A&A, 500, 725
Hovde, D. C., & Saykally, R. J. 1987, J. Chem. Phys., 87, 4332
Jin, C., Garrett, M. A., Nair, S., et al. 2003, MNRAS, 340, 1309
Kawaguchi, K., Muller, S., Black, J. H., et al. 2016, ApJ, 822, 115
Koopmans, L. V. E., & de Bruyn, A. G. 2005, MNRAS, 360, L6
Lidman, C., Courbin, F., Meylan, G., et al. 1999, ApJ, 514, L57
Lodders, K. 2003, ApJ, 591, 1220
Lucas, R., & Liszt, H. 1998, A&A, 337, 246
Martí-Vidal, I., Vlemmings, W., Muller, S., & Casey, S. 2014, A&A, 563, A136
Menten, K. M., Wyrowski, F., Belloche, A., et al. 2011, A&A, 525, A77
Morris, P. W., Gupta, H., Nagy, Z., et al. 2016, ApJ, 829, 15
Muller, S., & Guélin, M. 2008, A&A, 491, 739
Muller, S., Guélin, M., Dumke, M., et al. 2006, A&A, 458, 417
Muller, S., Beelen, A., Guélin, M., et al. 2011, A&A, 535, A103
Muller, S., Beelen, A., Black, J. H., et al. 2013, A&A, 551, A109
Muller, S., Combes, F., Guélin, M., et al. 2014a, A&A, 566, A112
Muller, S., Black, J. H., Guélin, M., et al. 2014b, A&A, 566, A6
Muller, S., Müller, H. S. P., Black, J. H., et al. 2016, A&A, 595, A128
Müller, H. S. P. 2010, A&A, 514, L6
Müller, H. S. P., Thorwirth, S., Roth, D. A., & Winnewisser, G. 2001, A&A, 370, L49
Müller, H. S. P., Schlöder, F., Stutzki, J., & Winnewisser, G. 2005, J. Mol. Struct., 742, 215
Müller, H. S. P., Goicoechea, J. R., Cernicharo, J., et al. 2014, A&A, 569, L5
Müller, H. S. P., Muller, S., Schilke, P., et al. 2015a, A&A, 582, L4
Müller, H. S. P., Kobayashi, K., Takahashi, K., Tomaru, K., & Matsushima, F. 2015b, J. Mol. Spectr., 310, 92
Nagy, Z., Van der Tak, F. F. S., Ossenkopf, V., et al. 2013, A&A, 550, A96
Nair, S., Jin, C., & Garrett, M. A. 2005, MNRAS, 362, 1157
Neufeld, D. A., & Wolfire, M. G. 2016, ApJ, 826, 183
Neufeld, D. A., Godard, B., Gérin, M., et al. 2015, A&A, 577, A49
Porras, A. J., Federman, S. R., Welty, D. E., & Ritchey, A. M. 2014, ApJ, 781, L8
Ritchey, A. M., Federman, S. R., & Lambert, D. L. 2011, ApJ, 728, 36
Ritchey, A. M., Welty, D. E., Dahlstrom, J. A., & York, D. G. 2015, ApJ, 799, 197
Roueff, E., Loison, J. C., & Hickson, K. M. 2015, A&A, 576, A99
Savage, C., Apponi, A. J., & Ziurys, L. M. 2004, ApJ, 608, L73
Schilke, P., Neufeld, D. A., Müller, H. S. P., et al. 2014, A&A, 566, A29
Schulz, A., Henkel, C., Menten, K. M., et al. 2015, A&A, 574, A108
Senekowitsch, J., Werner, H.-J., Rosmus, P., Reinsch, E.-A., & O'Neil, S. V. 1985, J. Chem. Phys. 83, 4661
Welty, D. E., Federman, S. R., Gredel, R., Thorburn, J. A., & Lambert, D. L. 2006, ApJS, 165, 138
Wiklind T., & Combes F. 1996, Nature, 379, 139
Winn, J. N., Kochanek, C. S., McLeod, B. A., et al. 2002, ApJ, 575, 103
Zanchet, A., Agúndez, M., Herrero, V. J., Aguado, A., & Roncero, O. 2013, AJ, 146, 125

Appendix A: Complementary laboratory data

We have evaluated the SH^+ spectroscopic parameters in the present work. Transition frequencies with microwave accuracy exist only for the $N = 1$–0 rotational transition; all the following data, including multiple determinations, were used in the present fit. Savage et al. (2004) reported data for the $J = 0-1$ and $J = 2-1$ fine structure (FS) components. Müller et al. (2014) analyzed ALMA data of the Orion Bar region and showed that the $J = 0-1$ datum of Savage et al. (2004) was in error by several megahertz and reported both hyperfine structure (HFS) components. Halfen & Ziurys (2015) obtained improved transition frequencies for all three FS components and confirmed the findings from ALMA observations (Müller et al. 2014). Even though Halfen & Ziurys (2015) only fit their own data, their fit displayed large residuals (up to 204 kHz) between measured transition frequencies and those calculated from their spectroscopic parameters much larger than the experimental 50 kHz. Exchanging the transition frequency of the $J = 1-1$, $F = 0.5$–0.5 HFS component at 683 359.227 MHz with that of a nearby line at 683 360.577 MHz yielded residuals of less than 20 kHz on average. Consequently, we employed the latter frequency in our fits. Brown & Müller (2009) derived extrapolated zero-field frequencies from laser magnetic resonance data (Hovde & Saykally 1987); in addition, rovibrational data (Brown et al. 1986; Civiš et al. 1989) were also used in the fit. The resulting parameters are given in Table A.1. We summarize for convenience the $N = 1$–0 transition frequencies determined with microwave accuracy in Table A.2. The re-evaluated SH^+ spectroscopic parameters will be used to create an updated entry for the CDMS catalog (Müller et al. 2001, 2005).

Table A.1. Spectroscopic parameters[a] (MHz, cm^{-1}) of sulfanylium, SH^+.

Parameter	Value
Y_{10}[b]	2547.4950 (104)
Y_{20}[b]	−49.4296 (90)
Y_{30}[b]	0.2098 (30)
$Y_{40} \times 10^3$[b]	−16.03 (34)
Y_{01}	278 095.11 (36)
Y_{11}	−8 577.42 (85)
Y_{21}	16.18 (32)
Y_{02}	−14.7431 (68)
$Y_{12} \times 10^3$	123.7 (26)
$Y_{03} \times 10^3$	0.46[c]
λ_{00}	171 489.6 (57)
λ_{10}	−473.0 (145)
λ_{20}	−78.6 (67)
λ_{01}	−1.35 (17)
γ_{00}	−5036.46 (89)
γ_{10}	116.5 (20)
γ_{20}	3.52 (64)
γ_{01}	0.433 (35)
$b_{F,0}(^1H)$	−56.840 (32)
$b_{F,1}(^1H) - b_{F,0}(^1H)$	−3.51 (79)
$c(^1H)$	33.482 (134)

Notes. [(a)] Numbers in parentheses are one standard deviation in units of the least significant digits. [(b)] In units of cm^{-1}. [(c)] Kept fixed to value derived by Brown & Müller (2009).

Table A.2. Quantum numbers J and F, frequencies (MHz), uncertainties (Unc., kHz), and residuals o−c (kHz) between observed rest frequencies obtained with microwave accuracy used in the present fit and those calculated from the present set of spectroscopic parameters of the $N = 1$–0 transition of sulfanylium, SH^+, and notes on the source.

$J' - J''$	$F' - F''$	Frequency	Unc.	o−c	Note
0−1	0.5−0.5	345 858.271	50	24	*a*
0−1	0.5−0.5	345 858.270	200	23	*b*
0−1	0.5−1.5	345 944.420	50	−21	*a*
0−1	0.5−1.5	345 944.350	200	−50	*b*
2−1	1.5−0.5	526 038.793	50	7	*a*
2−1	1.5−0.5	526 038.722	75	−64	*c*
2−1	2.5−1.5	526 048.023	50	23	*a*
2−1	2.5−1.5	526 047.947	75	−53	*c*
2−1	1.5−1.5	526 124.951	50	12	*a*
2−1	1.5−1.5	526 124.976	75	37	*c*
1−1	1.5−0.5	(683 334.681)	67	–	*d*
1−1	0.5−0.5	683 360.577	50	5	*e*
1−1	1.5−1.5	683 420.835	50	2	*a*
1−1	0.5−1.5	(683 446.724)	67	–	*d*

Notes. [(a)] Halfen & Ziurys (2015). [(b)] Müller et al. (2014). [(c)] Savage et al. (2004). [(d)] Frequencies and uncertainties calculated from the spectroscopic parameters in Table A.1. [(e)] This work and Halfen & Ziurys (2015).